Journal of
Materials Chemistry A

Materials for energy and sustainability

Accepted Manuscript

This article can be cited before page numbers have been issued, to do this please use: A. Gupta, S. Ghosh, D. Bhalothia, J. Chowdhury and S. Pande, *J. Mater. Chem. A*, 2026, DOI: 10.1039/D6TA00849F.

ROYAL SOCIETY OF CHEMISTRY

rsc.li/materials-a

View Article Online
DOI: 10.1039/D6TA00849F

Enhanced Activity and Durability of Ir Single Atom Catalyst for Electrocatalytic Oxygen Evolution Reaction Through Synergistic Electronic Coupling with Co_3O_4 Matrix

Astha Gupta[a], Swarup Ghosh[b], Dinesh Bhalothia[c*], Joydeep Chowdhury[d], and Surojit Pande[a*]

[a]Department of Chemistry, Birla Institute of Technology and Science, Pilani, Rajasthan-333031, India

Corresponding author: Surojit Pande, E-mail: spande@pilani.bits-pilani.ac.in

[b]School of Computer Science and Artificial Intelligence, SR University, Warangal, Telangana 506371, India.

[c]Department of Electronics and Communication Engineering, Manipal University Jaipur, Rajasthan 303007, India

[d]Department of Physics, Jadavpur University, 188, Raja S.C. Mallick Road, Kolkata, 700032, India.

View Article Online
DOI: 10.1039/D6TA00849F

Abstract

Single atom catalysts (SACs), owing to their high activity, selectivity, and 100 % atom utilization properties, show a great potential for heterogeneous catalysis. However, it is still a challenge to synthesize SACs because of their poor stability and tendency to aggregate. In this regard, we propose an approach to synthesize a stable Ir single atom catalyst on Co_3O_4 substrate using hydrothermal technique followed by calcination. The XAS and XPS analysis reveals the strong electronic coupling between the Ir SAC and support matrix, which stabilizes the single atoms via formation of Ir-O and Ir-Co bond pairs. The strong electronic interaction results into enhanced density of unoccupied d-orbitals of Ir single atoms, and higher valence state of Co atoms, both synergistically improved the electrocatalytic activity. HAADF-STEM images confirm the isolated homogenous distribution of Ir single atoms on the Co_3O_4 matrix. The synthesized catalyst, Ir_{SAC}-Co_3O_4 shows improved activity for electrocatalytic oxygen evolution reaction (OER) in 1 M KOH, with an overpotential of 270 mV, and a Tafel slope value of 76 mV/dec. Ir_{SAC}-Co_3O_4 catalyst exhibits high electrocatalytic durability up to 96 hours at an elevated current density of 130 mA/cm^2, demonstrating robust electronic interaction of single atoms with the support matrix, that prevents the aggregation of single atoms. Post-electrocatalytic XPS analysis reveals no substantial change in the valence state, which can be further accredited to the electronic coupling between the support and the single atom. DFT finding demonstrates that the presence of Ir single atom promotes the OER kinetics by stabilizing the key reaction intermediates and lowering the overpotential of rate-determining step.

Key words: Single atom catalysts, Oxygen evolution reaction, Synergistic effect, Metal-support interaction, and Density functional theory

View Article Online
DOI: 10.1039/D6TA00849F

Introduction:

In the current context, the most extensive energy conversion sources are fossil fuels. This excessive dependence not only causes their exhaustion but also raises environmental concerns. To solve this issue, we need to look after towards cleaner, abundant and reasonable energy sources. In this context, one of the most renowned approach for producing renewable and sustainable energy is electrocatalytic water splitting, which generates hydrogen and oxygen.[1, 2] The OER process involves a multi-step, four-electron exchange procedure includes a complex mechanism that involves O–O coupling and O–H bond breaking, which makes it sluggish in nature compared to the HER, which involves a two-electron transfer procedure. Thus, the overall productivity of electrocatalytic water splitting suffers from the slow reaction kinetics of anodic OER, which leading to substantial energy loss, necessitating the design of an efficient OER electrocatalyst. Currently, IrO_2 and RuO_2 are the most extensively employed commercial electrocatalyst for OER, but the scarcity and poor stability limit their widespread application.[3-5] Consequently, many efforts have been carried out to develop an affordable alternative electrocatalyst for OER, such as transition metal-based oxides[6, 7] or hydroxides,[8, 9] sulphides,[10, 11] phosphides,[12, 13]selenides[14], and perovskite oxides.[15, 16] Nevertheless, their catalytic activity is inadequate and far less than the standard, requiring refinement to obtain substantial efficiency.

Single-atom catalysts (SACs) have engrossed much consideration due to their electrocatalytic performance in heterogeneous catalysis for many advantages, such as enhanced homogeneity of active sites, elevated activity, and maximum atom utilization.[17-21] Furthermore, the unsaturated coordination state of isolated atoms maximizes metal atom utilization, and lowers the reaction energy barrier, thereby promoting efficient adsorption and activation of reactant molecules. However, the synthesis of SACs remains challenging due to their low metal loading and poor stability, leading to the aggregation of isolated atoms into either a nanoparticle or a cluster.[22, 23] These isolated atoms can be mounted to a variety of supports, such as carbon-based materials,[24] metal phosphides,[25] layered double hydroxides[26] and metal oxides.[27]

Compared to the other types of support matrix, metal oxides have received extensive attention because of their distinctive properties, such as their high stability, oxygen vacancy, defect sites.[28, 29] These sites work as anchored points for isolated atoms and provide strong metal-support interaction through the formation of M-M and M-O bonds between the isolated atoms and the metal oxide support matrix.[30, 31] Moreover, under OER conditions, transition metal oxide supports

View Article Online
DOI: 10.1039/D6TA00849F

can undergo dynamic surface reconstruction, leading to the formation of catalytically active (oxy)hydroxide layers. These reconstructed species are often considered the true active phase.[32, 33] The presence of single atoms may facilitate this reconstruction process, which further contribute in enhanced electrocatalytic activity.[34] In this regard, Kumar and co-workers[34] synthesized an Ir single atom on NiO support, which exhibited a 256 mV overpotential value to generate a 10 mA/cm^2 current density. The isolated Ir atoms are partly embedded on NiO substrate via forming the Ir-O and Ir-Ni bond that provides the structural rigidity and prevent aggregation of Ir single atoms. Moreover, under operating conditions, the active structure of the electrocatalyst was analyzed by in situ Raman spectroscopy, which reveals the formation of NiOOH for both NiO and Ir-decorated NiO. The formation of NiOOH takes place at a much lower potential for the Ir-decorated NiO in contrast to the pristine NiO, suggesting the metal-support interaction among the NiO support and isolated Ir atoms. Yang and co-workers[35] developed an Ir single-atom catalyst over oxygen-vacant $CoNiO_2$ support as an effective electrocatalyst for OER. The Ir single atoms show a higher valence state and form an Ir-O covalent bond, resulting in substantial overlay of 5d and 2p bands of Ir and O, respectively, which boosts the O_2 evolution by accelerating the conversion from O-O to OO* by following the lattice oxygen mechanism pathway. Cai and co-workers[36] reported Ir single atoms supported on CoO_x nanosheets for OER. The Ir atoms captured by surface-absorbed oxygen form an Ir-O-Co bond, stabilizing the isolated Ir atoms and promoting the electrocatalytic OER. Shan and co-workers[37] synthesized Ir single atoms that integrated into Co_3O_4 spinel ($Ir_{0.06}Co_{2.94}O_4$) for an efficient electrocatalyst for OER in 0.1 M $HClO_4$. Single atoms integrated into the Co_3O_4 via an ion interchange process, subsequently by calcination using ZIF-67 as a source for Co_3O_4, and observed an onset potential of 1.45 V *vs.* RHE, with high mass activity of 2511 A g^{-1}. The cooperative contribution of nano domains, containing Ir in octahedral sites with in enclosure of the Co sites, is attributed to the elevated activity. Incorporation and stabilization of Ce single atom on Co_3O_4 support via Ce-O bond, reported by Zhao and co-workers[38] for OER in acidic medium. The synthesized electrocatalyst exhibits an onset potential of 1.57 V *vs.* RHE at 10 mA/cm^2 current density. The increased charge transportation and modified electronic environment post Ce single atom incorporation to Co_3O_4 were attributed to enhanced activity. According to the literature described above, anchoring metal isolated atoms on a metal oxide support can effectively improve the electrocatalytic OER activity.

View Article Online
DOI: 10.1039/D6TA00849F

Inspired by the previous reports, we synthesized Ir single atoms supported on Co_3O_4 on carbon cloth (CC) via a hydrothermal process followed by pyrolysis. The synthesized catalyst demonstrated elevated performance for OER in 1.0 M KOH. Pristine Co_3O_4 and single-atom decorated samples were intensively characterized using various techniques such as X-ray diffraction (XRD), high-angle annular dark field spectroscopy (HAADF-STEM), X-ray absorption spectroscopy (XAS), and X-ray photoelectron spectroscopy (XPS). The optimized Ir SAC on Co_3O_4 showed the superior electrocatalytic OER activity in alkaline medium, achieving a 10 mA/cm^2 current density at an onset potential of 1.51 V *vs.* RHE, and a low Tafel slope value, 76 $mVdec^{-1}$. The following points briefly describe the positive outcome of this work: First, the formation method is simple and easy to comprehend, resulting in a 3.04 wt% Ir single atom loading on Co_3O_4 support. Second, the enhanced activity result of faster charge transfer can be attributed to the synergistic electronic coupling between the Ir single atoms and the Co_3O_4 substrate. Third, the as-synthesized Ir_{SAC}-Co_3O_4 shows remarkable stability in OER. Fourth, the DFT results unveil the metallic character for Ir_{SAC}-Co_3O_4 with zero band gap after the introduction of Ir, which facilitates the charge transfer and subsequently improves the electrocatalytic activity.

2. Experimental Section

2.1. Synthesis of Co_3O_4

The synthesis of Co_3O_4 involved a hydrothermal method followed by calcination. First, $Co(NO_3)_2.6H_2O$ (0.6 g) and NH_2CONH_2 (0.6 g) were mixed in 30 mL of Milli-Q water. The entire solution was then transferred to the autoclave. The carbon cloth was cut into a suitable shape (4 × 3 cm) and placed in the autoclave to undergo an 8-hour hydrothermal reaction at 95 ^{0}C. In the first step, a metal-carbonate hydroxide precursor ($Co(CO_3)_x(OH)_y.H_2O$) was developed over the CC surface. After washing with water and ethanol, the as-deposited CC was dried for 8 h at 50 ^{0}C. The resulting carbonate precursor grown on CC was calcined for 3 h at 350 °C in a muffle furnace to yield Co_3O_4 and used as a pristine sample.

2.2 Synthesis of Ir_{SAC}-Co_3O_4

The synthesis of single-atom Ir-doped Co_3O_4 was completed in two steps. The $Co(CO_3)_x(OH)_y.H_2O$ precursor was initially synthesized over CC by following the hydrothermal

View Article Online
DOI: 10.1039/D6TA00849F

method as discussed above. In the second step, the metal-carbonate hydroxide complex deposited over CC was impregnated into a solution of $IrCl_3.xH_2O$ (3.15×10^{-2} M or 10 mg/mL) for 10 minutes, followed by drying and calcination at 350 ^{0}C for 3 h, to obtain Ir single atom doped Co_3O_4 (Ir_{SAC}-Co_3O_4). The amount of Ir precursor was optimized by varying the concentration of $IrCl_3.xH_2O$ solution (5 mg/mL, 15 mg/mL, 20 and 25 mg/mL), where the other reactant remains unchanged. ICP analysis of all the samples obtained by varying the concentration of the Ir precursor solution is presented in Table S1 (Supporting Information). The data indicate that the Ir weight percentage on Co_3O_4 increases with increasing concentration of $IrCl_3$ solution. The optimized sample exhibits an Ir content of 3.02 wt%.

2.3 Electrochemical measurements

The electrocatalytic activity of Ir_{SAC}-Co_3O_4 and Co_3O_4 was evaluated in 1 M KOH by a three-electrode system. The working electrode was made with sample-obtained (Co_3O_4 and Ir_{SAC}-Co_3O_4) on CC, while Ag/AgCl and graphite rod were used as the reference and counter electrode, respectively. The working electrode area (0.4 × 0.4 cm2) was fixed by applying epoxy paste on the sample-deposited CC. The catalyst loading of Ir_{SAC}-Co_3O_4 and Co_3O_4 was 0.28 mg. All electrochemical investigations were performed using the CHI604E instrument. At a scan rate of 2.0 mV/s, and a potential window of 0 to 0.8 V for OER *vs.* Ag/AgCl was employed for the linear sweep voltammetry (LSV) analysis. The formula $E_{RHE} = E_{Ag/AgCl} + 0.0591\ pH + E^0_{Ag/AgCl}$ was employed to convert the potential of the Ag/AgCl reference electrode to the RHE scale. In the electrochemical impedance spectroscopy (EIS) analysis of Ir_{SAC}-Co_3O_4 and pristine Co_3O_4, the onset potential was used as an operational bias for data recording.

3. Results and Discussion

3.1. Mechanism for the synthesis

The experimental section explained the complete synthesis of Ir single atoms anchored over Co_3O_4. In the first step, i.e., hydrothermal process, the metal-carbonate hydroxide precursor ($Co(CO_3)_x(OH)_y.H_2O$) is formed. First, the hydrolysis of urea released CO_3^{2-} and OH^-, which then react with the Co^{2+} and form metal-carbonate hydroxide precursor. In the second step, the metal-carbonate hydroxide precursor was converted into Co_3O_4 by calcination for 3 h at 350 ^{0}C. To

View Article Online
DOI: 10.1039/D6TA00849F

synthesize Ir_{SAC}-Co_3O_4, the metal-carbonate-hydroxide complex was impregnated into the $IrCl_3.xH_2O$ solution to enable the electrostatic adsorption of Ir-ions on the precursor surface, then drying and calcination for 3 h at 350 ^{0}C. The overall synthesis strategy for Ir_{SAC}-Co_3O_4 is given in Scheme 1. The plausible reaction mechanism involved in the formation of Co_3O_4 is as follows:

$$H_2NCONH_2 + H_2O \rightarrow 2NH_3 + CO_2$$

$$NH_3 + H_2O \rightarrow NH_4^+ + OH^-$$

$$CO_2 + H_2O \rightarrow CO_3^{2-} + 2H^+$$

$$Co^{+2} + xCO_3^{2-} + y^-OH + H_2O \rightarrow Co(CO_3)_x(OH)_y.H_2O$$

$$Co(CO_3)_x(OH)_y.H_2O \xrightarrow{\Delta} Co_3O_4 + xCO_2 + yH_2O$$

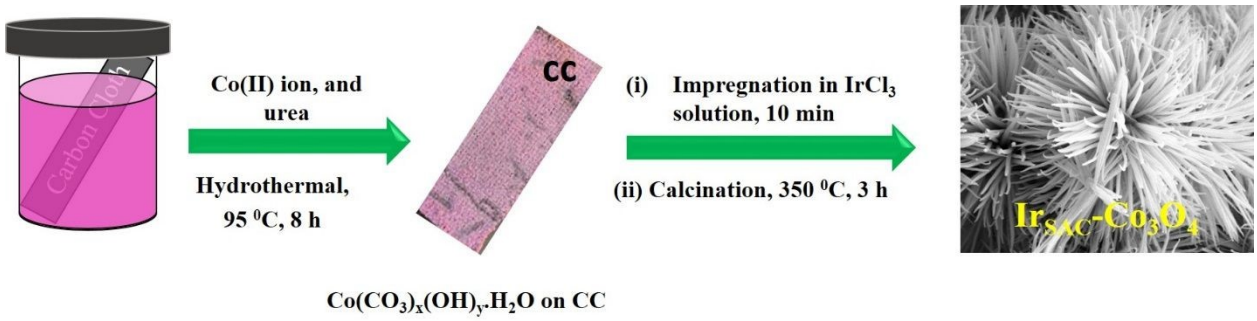

Scheme 1: Schematic presentation for the synthesis of Ir_{SAC}-Co_3O_4 on CC

3.2. Material characterization for structural analysis

The phase purity and crystallinity of pristine Co_3O_4 and Ir_{SAC}-Co_3O_4 samples are confirmed by XRD analysis. The distinct and prominent diffraction peaks for both samples (Fig. S1) are consistent with the cubic phase of Co_3O_4 (JCPDS 00-042-1467) with cell parameters a = b = c = 8.07 Å and $\alpha = \beta = \gamma = 90^o$. The well-matched diffraction patterns indicate the formation of a pure phase in the synthesized samples. A broad peak at 25 ^{o} is observed corresponding to the CC. The diffraction angles of Ir_{SAC}-Co_3O_4 sample show no significant change or shift, suggesting that Ir single atoms are not altering the lattice parameters and crystal structure of Co_3O_4. Moreover, no diffraction peaks for Ir and IrO_2 are observed in the Ir_{SAC}-Co_3O_4 sample, indicating the absence of both metallic Ir and IrO_2.

View Article Online
DOI: 10.1039/D6TA00849F

The morphology of both pristine Co_3O_4 and Ir_{SAC}-Co_3O_4 samples is analyzed by FESEM. The FESEM images of the pristine sample at various resolutions are shown in Fig. S2a and b that reveal the uniformly distributed nanoflower morphology throughout the carbon cloth. The synthesized nanoflower are composed of thin nanorods of thickness reaching from 100 to 400 nm along with rough morphology. Fig. 1a and b show FESEM images of Ir single atom-doped Co_3O_4 sample at low and high resolution, confirming the retention in morphology. Thus, the uniform distribution of nanoflower morphology along with a rough surface ensures the complete exposure of catalytic sites and efficient contact between the electrode and electrolyte. FESEM images of other samples synthesized using various concentrations of $IrCl_3$ solution are given in Fig. S2 (c-h). The morphology of all the samples remained similar across varying concentrations of the $IrCl_3$ solution. This indicates that the amount of $IrCl_3$ does not influence the morphology of the material. The SEM-EDS mapping analysis of Ir/Co_3O_4 samples with varying Ir concentrations is presented in Table S2. The results indicate a uniform distribution of Ir elements with increased concentration.

To further confirm the morphology and crystallinity of pristine Co_3O_4 and Ir_{SAC}-Co_3O_4, TEM and HRTEM analyses are performed. TEM image of Co_3O_4 (Fig. S3a and b) verifies the nanoflower morphology. The d-spacing value of the (311) plane is calculated to be 0.24 nm for the of pristine Co_3O_4 sample (Fig. S3c). The TEM image (Fig. S3d and e) of the Ir single atom doped sample shows similar nanoflower morphology made of nanorods. The atomic dispersion of Ir single atoms over Co_3O_4 support is confirmed by HAADF-STEM images. As shown in Fig. 1c, d, and e, the isolated bright spots corresponding to Ir atoms are uniformly distributed across the entire Co_3O_4 support matrix, showing the successful synthesis of Ir single atoms without any aggregation. HAADF-STEM element mapping analysis (Fig. 1f) further validates the uniform atomic distribution of Ir single atoms over the CO_3O_4 surface. Additionally, HAADF-STEM analysis of the Ir/Co_3O_4 sample containing the highest wt% (4.91 %) of Ir was also performed. Fig. 1g and h show the bright spots in aggregate form, indicating the formation of an Ir cluster on Co_3O_4 support ($Ir_{cluster}$-Co_3O_4). The aggregated form of Ir cluster is further verified by EDS mapping analysis (Fig. 1i). This observation demonstrates the transition from atomically dispersed Ir to aggregation in cluster form with increasing wt% of Ir.

View Article Online
DOI: 10.1039/D6TA00849F

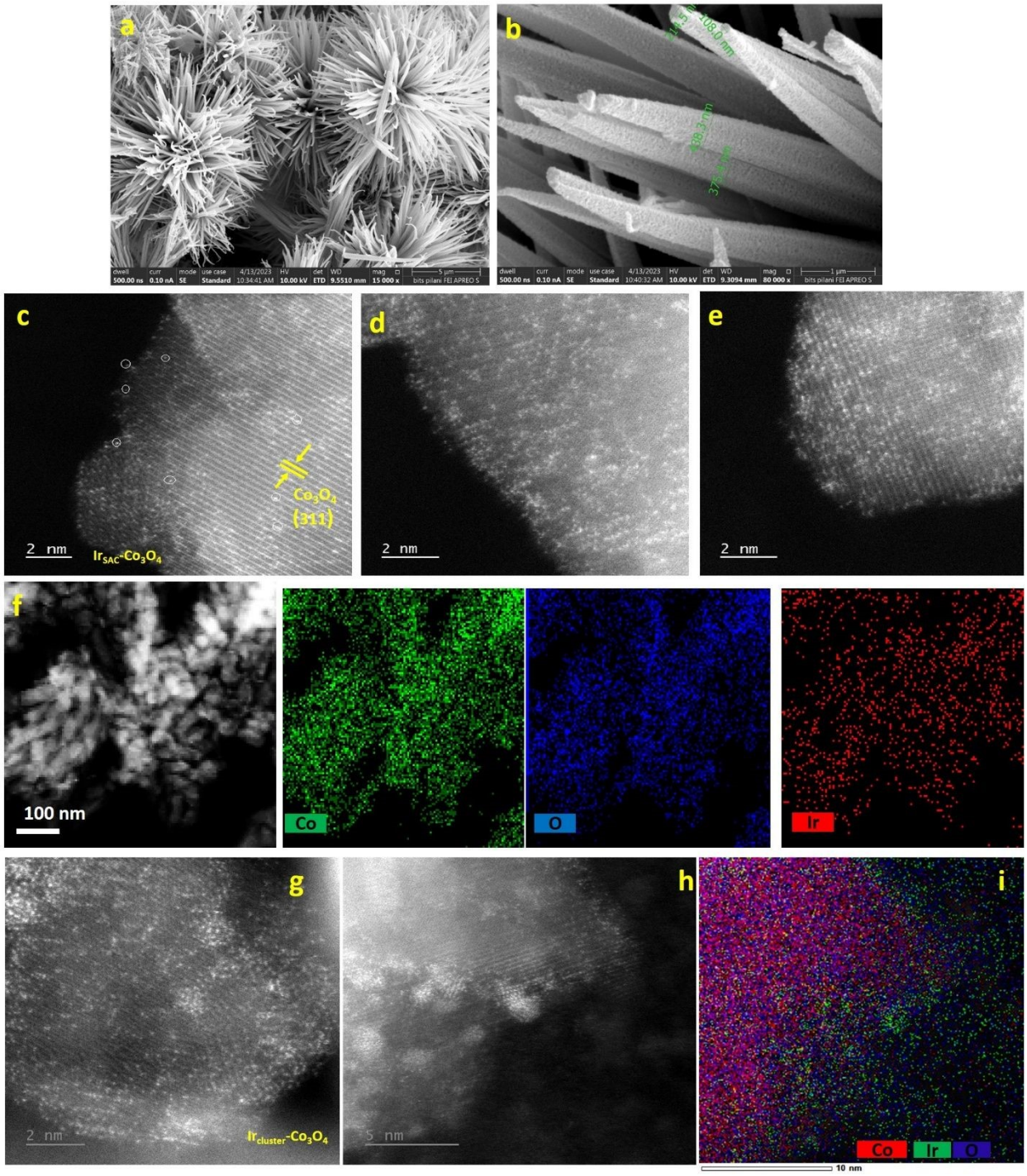

Fig. 1. FESEM images at low and high resolution (a and b), HAADF-STEM images with the optimized concentration of Ir is 10 mg/mL (c, d, and e), and corresponding STEM elemental mapping (f) of Ir_{SAC}-Co_3O_4. HAADF-STEM images, where Ir concentration is 25 mg/mL (g and h), and (i) element mapping for $Ir_{cluster}$-Co_3O_4.

View Article Online
DOI: 10.1039/D6TA00849F

In order to have insight into the valence state and local coordination environment, the X-ray near-edge fine structure (XANES) and extended X-ray absorption fine structure (EXAFS) spectra were employed for Ir-Co_3O_4 sample, commercial IrO_2 and Ir foil were used as benchmarks. Fig. 2a shows the normalized XANES spectrum at the Ir L_3-edge for Ir_{SAC}-Co_3O_4 along with IrO_2 and Ir foil for reference. The intensity of the white line/spectral line intensity (H_A) of Ir L_3-edge spectrum represents the density of unoccupied Ir-d orbitals and the extent of surface chemisorption of oxygen.[39, 40] Remarkably, the high intensity of the white line for Ir-Co_3O_4 compared to Ir foil indicates the increased density of unoccupied orbitals of Ir atoms.[41] That explains the superior performance of Ir-Co_3O_4 for electrocatalytic OER, since an increased density of unoccupied orbitals promotes the electrocatalytic efficiency. Furthermore, the shift in the inflection point (I_P) indicates the higher threshold energy (E_0) of Ir_{SAC}-Co_3O_4 compared to the Ir-foil, which validates the depletion of the Ir-d band. The higher surface oxygen chemisorption and depletion of the d-band of Ir present in the Ir-Co_3O_4 sample further suggest the existence of Ir single atoms.[42] Additionally, the position of the inflection point (I_P) of Ir_{SAC}-Co_3O_4 lies between the Ir foil and IrO_2, which indicates the partial oxidation of Ir atoms in the Ir_{SAC}-Co_3O_4 sample. The bonding of Ir single atoms with the Co and O atoms of the support matrix can be attributed to the positive shift in the threshold energy (E_0), and the partial oxidation state of Ir atoms in Ir_{SAC}-Co_3O_4

The Fourier transforms EXAFS (FT-EXAFS) spectra of Ir_{SAC}-Co_3O_4, along with the reference sample (Ir foil and IrO_2) at the Ir L_3-edge, are shown in Fig. 2b. The related parameters for the quantitative structure of both Co_3O_4 and Ir_{SAC}-Co_3O_4 are summarized in Table S3. As evident, the Ir-Ir scattering path appears at 2.51 Å is corresponding to the Ir foil. For Ir_{SAC}-Co_3O_4 sample, the peak corresponding to the Ir-Ir scattering is absent, and also the zero-coordination number (CN) for Ir-Ir bond pair (Table S3) firmly substantiates the formation of Ir single atoms on Co_3O_4 support. The peak across the 1.0 to 3.0 Å corresponds to the Ir-O and Ir-Co bond pairs with a $CN_{Ir\text{-}O} = 3.01$ and $CN_{Ir\text{-}Co} = 2.16$, respectively. The reduced coordination of 3.01 for the Ir-O bond, in contrast to the expected CN = 6 for standard IrO_2, further validates the partial oxidation of Ir single atoms. Wavelet transform (WT) analysis provides additional insights into the structural characteristics. As illustrated in Fig. 2c, the Ir_{SAC}-Co_3O_4 catalyst does not show the peak corresponding to the Ir-Ir bond pair, further strengthening the presence of Ir-single atoms.

The chemical state of Co is also investigated by Co k-edge XAS analysis. The XANES spectra of Ir-Co_3O_4, pristine Co_3O_4, along with Co foil, are shown in Fig. 2d, which includes

View Article Online
DOI: 10.1039/D6TA00849F

essential characteristics such as inflection point (I_P). The positive shift in the inflection point (I_P) for Ir_{SAC}-Co_3O_4 compared to the pristine Co_3O_4 suggests a higher valence state of Co, ascribed to the electron transfer from Co to Ir through Ir-Co bonding. Furthermore, the FT-EXAFS spectrum reveals the coordination environment of Co-atoms. As shown in Fig. 2e, both Ir_{SAC}-Co_3O_4 and Co_3O_4 show similar FT-EXAFS profiles, indicating the Ir single atoms do not affect the local structure of Co_3O_4 lattice. Furthermore, the WT pattern of both Co_3O_4 and Ir_{SAC}-Co_3O_4 exhibits a missing peak intensity at 2.01 Å, which belongs to the Co-Co bond pair in Co foil, indicating the total oxidation of Co atoms in both samples (Fig. 2f). The overlay spectra of Ir-Co_3O_4 EXAFS and corresponding fitting is given in Fig. S4a.

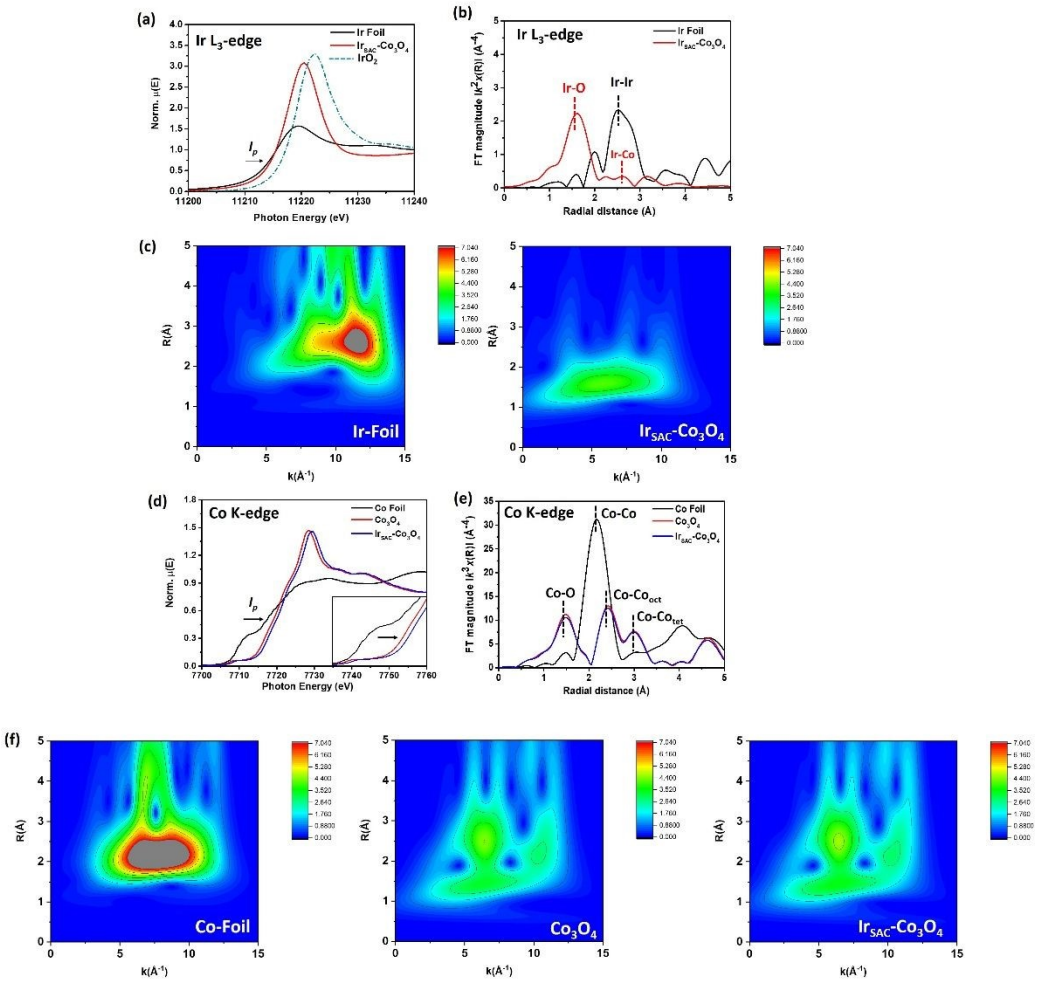

Fig. 2. X-ray absorption spectroscopy. (a) XANES, (b) FT-EXAFS spectra and (c) WT patterns at Ir L_3-edge for Ir_{SAC}-Co_3O_4 along with reference samples. (d) XANES, (e) FT-EXAFS spectra and (f) WT patterns at Co K-edge for Ir_{SAC}-Co_3O_4 and reference samples.

View Article Online
DOI: 10.1039/D6TA00849F

XPS analysis was performed to further assess the valence and chemical state of all elements in both the Co_3O_4 and Ir_{SAC}-Co_3O_4 samples. Fig. S4b, c, and d demonstrate the survey and deconvoluted spectra of Co 2p and O 1s, respectively, for the pristine Co_3O_4 sample.

The deconvoluted XPS spectra of Co 2p exhibit two doublets along with three satellite peaks (Fig. S4c). The binding energy (BE) value of the doublets corresponding to the Co $2p_{3/2}$ is 779.37 and 780.81 eV, indicating the presence of Co^{3+} and Co^{2+}, respectively. Another doublet peak for the Co $2p_{1/2}$ state appeared at 794.31 and 795.75 eV, corresponding to the Co^{3+} and Co^{2+}, respectively. Three peaks can be seen in the O 1s deconvoluted XPS spectra (Fig. S4d): O1 (positioned at 529.52 eV), O2 (530.90 eV), and O3 (532.24 eV). The metal-oxygen bond or lattice oxygen is attributed to the peak at O1. The peak O2 associated with the O-vacancy, oxygen in absorbed water, is the cause of the O3 peak. All of the BE values of Co and O are well matched with the literature.[43, 44]

Moreover, the presence of Ir and other ions in the Ir_{SAC}-Co_3O_4 sample was verified further with XPS survey scan (Fig. 3a). The deconvoluted Co 2p spectra reveal two prominent groups of spin-orbit coupling peaks (Fig. 3b). The peaks at 779.98 and 795.07 eV represent the Co^{3+} ions in the Co $2p_{3/2}$ and Co $2p_{1/2}$ states, respectively. Another two pairs of Co^{2+} are located at 781.40 and 796.68 eV, corresponding to Co $2p_{3/2}$ and Co $2p_{1/2}$. A substantial electronic interaction between the Ir single atoms and the support atoms is shown by the binding energy values of Co 2p in the Ir_{SAC}-Co_3O_4, which exhibit a positive shift of approximately 0.63 eV compared to the pure sample. The three satellite peaks are positioned at 784.82 and 788.93 eV, corresponding to Co^{2+} and Co^{3+} for the Co $2p_{3/2}$ shake-up satellite, respectively, while another peak at 804.41 eV corresponds to the shake-up satellite peak of Co^{3+} for Co $2p_{1/2}$. The XPS spectra of O 1s are deconvoluted into three peaks (Fig. 3c). Peak O2 at 531.53 eV corresponds to the O-vacancy, oxygen in lattice oxygen (M−O) at 530.28 eV, and in adsorbed water (O−H_2O) at 532.48 eV. The binding energy value of O 1s exhibits a positive shift of approximately 0.7 eV compared to the pure Co_3O_4, indicating a significant surface oxygen chemisorption following the insertion of an Ir single atom. The O-vacancy was further quantified, the obtained % O-vacancy in Co_3O_4, Ir_{SAC}-Co_3O_4 are 32.6 and 23.26, respectively. All the binding energy values for Co_3O_4 and Ir_{SAC}-Co_3O_4 are listed in Table S4.

The XPS spectra of Ir 4f is deconvoluted into three peaks (Fig. 3d). The peaks positioned at 62.39, 65.19, and 66.94 eV correspond to Ir $4f_{7/2}$, Ir $4f_{5/2}$, and satellite peak, respectively.

View Article Online
DOI: 10.1039/D6TA00849F

Furthermore, the peak appeared at 60.32 eV, corresponding to Co 3p. Higher BE energy of Ir single atoms in Ir_{SAC}-Co_3O_4 sample compared to the metallic Ir (60.8 eV) indicates that Ir atoms are highly oxidized, which aligns well with the Ir L_3-edge XANES result. Biswal and co-workers[45] observed the value of binding energies of Ir $4f_{7/2}$ in IrO_2 and $IrCl_3$ are 62.54 and 62.13 eV, respectively. The observed binding energy value (62.39 eV) of Ir $4f_{7/2}$ for the Ir_{SAC}-Co_3O_4 sample that falls between the binding energy values for metallic Ir (60.8 eV) and IrO_2 (62.54 eV), indicating the intermediate oxidation state of Ir single atoms that align well with the Ir L_3-edge XANES findings.

The enhanced valence state of Co atoms of substrate could be attributed to the highly oxidized Ir atoms over Co_3O_4, that acts as a Lewis acid and pulls the electron from nearby Co atoms. By calculating the area within the curve, the ratio of Co^{2+}/Co^{3+} is calculated for both Co_3O_4 and Ir_{SAC}-Co_3O_4, to confirm the electron-withdrawing nature of Ir atoms. The value of $Co^{2+/}Co^{3+}$ ratio for the Co_3O_4 sample is 0.43. On the other hand, the ratio in the Ir_{SAC}-Co_3O_4 sample is 0.39. The higher valence state of Co for Co_3O_4 is suggested by this lower value of the $Co^{2+/}Co^{3+}$ ratio, which further indicates a significant electronic interaction between the Co atoms and the single Ir atoms that results in electron relocation. The Co K-edge XANES study and the XPS analysis results are in well agreement. Strong electronic coupling between the single atom and the support matrix is thus represented by the positive shift in the binding energy values of both Co and oxygen as well as the enhanced valence state of Co in Ir_{SAC}-Co_3O_4 in comparison to the pristine Co_3O_4. Our group noticed a similar phenomenon of decreased Ni^{2+}/Ni^{3+} ratio following heteroatom doping.[46]

The formation of oxygen-vacancy further verified by electron paramagnetic resonance (EPR) analysis. Both pristine Co_3O_4 and Ir_{SAC}-Co_3O_4 samples exhibits clear signals in the EPR spectra (Fig. S5), indicating the presence of unpaired electrons associated with oxygen-vacancies. The measured g values (spectral splitting factor) are 1.91 and 1.93 for pristine Co_3O_4 and Ir_{SAC}-Co_3O_4, respectively. The coordination of Ir single atoms with O, regulates the oxidation state and basic catalytic properties of single atom catalysts. While the bonding of Ir with Co atoms of support matrix gives stability to the single atoms, which is reflecting in the durability during electrocatalytic OER.[28]

View Article Online
DOI: 10.1039/D6TA00849F

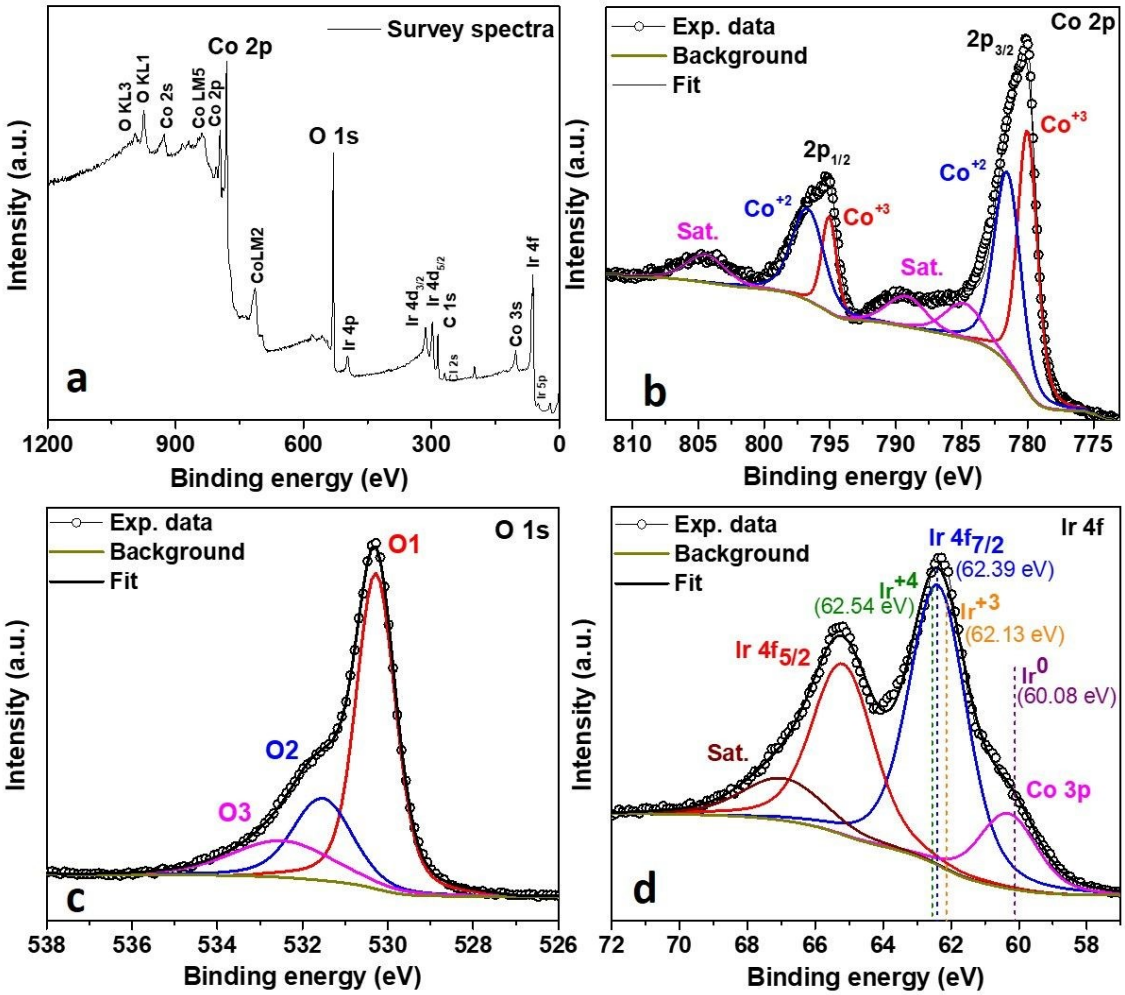

Fig. 3. XPS analysis of Ir_{SAC}-Co_3O_4 sample (a) survey spectrum, deconvoluted XPS spectra of (b) Co 2p, (c) O 1s, and (d) Ir 4f.

4. Electrocatalytic performance: OER study

The electrocatalytic activity of all the developed samples were assessed in 1 M KOH, using a three-electrode setup. The LSV analysis was recoded at a scan rate of 2 mV s^{-1}. OER performance of pristine Co_3O_4 and IrO_2 supported on CC was evaluated for comparison. The LSV polarization curve (Fig. 4a) shows that Ir_{SAC}-Co_3O_4 exhibited enhanced OER activity, requiring low overpotential (Ƞ) of only 270 mV to reach a current density of 10 mA/cm^2, that significantly

View Article Online
DOI: 10.1039/D6TA00849F

outperform the benchmark IrO_2 catalyst (η_{10}: 410 mV) and pristine Co_3O_4 (η_{10}: 350 mV). The substantially improved OER activity of Ir_{SAC}-Co_3O_4 can be attributed to the presence of Ir single atoms over Co_3O_4 support. The enhanced activity of Ir_{SAC}-Co_3O_4 can be seen by a histogram (Fig. 4b) that is plotted at 1.60 V *vs.* RHE for Ir_{SAC}-Co_3O_4, Co_3O_4 and IrO_2.

To optimize the amount of Ir, other samples were prepared using different concentration of $IrCl_3.xH_2O$. The onset potential to achieve 10 mA/cm^2 current density is lowest for the catalyst prepared by using 10 mg/mL concentration of Ir (Ir_{SAC}-Co_3O_4) and highest for the sample synthesized by using 25 mg/mL concentration of Ir ($Ir_{cluster}$-Co_3O_4) (Fig. S6). This result reveals that, despite the $Ir_{cluster}$-Co_3O_4 sample having a higher Ir loading of 4.91 wt%, its OER activity is inferior compared to the Ir_{SAC}-Co_3O_4 sample, which contains a lower Ir content of 3.02 wt%. The superior performance of Ir_{SAC}-Co_3O_4 demonstrates the high atom utilization efficiency of SACs, where atomically dispersed Ir atoms are more effectively involved in the catalytic process, resulting in higher catalytic activity compared to the higher Ir loading in the cluster-based counterpart.

The optimized concentration was further confirmed by TOF and mass activity analysis (Table S5). A comparative analysis of OER values reported in the literature is provided in Table S6. The high valence state of Ir atoms as a consequence of the robust electronic interaction from the support matrix, which exhibits an elevated density of unoccupied orbitals, also the enhanced valence state of Co atoms, together contribute to the improved OER activity of the Ir_{SAC}-Co_3O_4. Moreover, the superior OER performance of Ir_{SAC}-Co_3O_4 was corroborated by its higher mass activity, at a fixed potential of 1.55 V *vs.* RHE. The values of mass activity for Ir_{SAC}-Co_3O_4, Co_3O_4 and IrO_2 are 274.28, 35.74, and 35.71 A g^{-1}, respectively. Compared to pristine Co_3O_4, Ir_{SAC}-Co_3O_4 exhibits 8 times greater mass activity, indicating a significant electron transfer efficiency, as evidenced by its electrocatalytic activity.

View Article Online
DOI: 10.1039/D6TA00849F

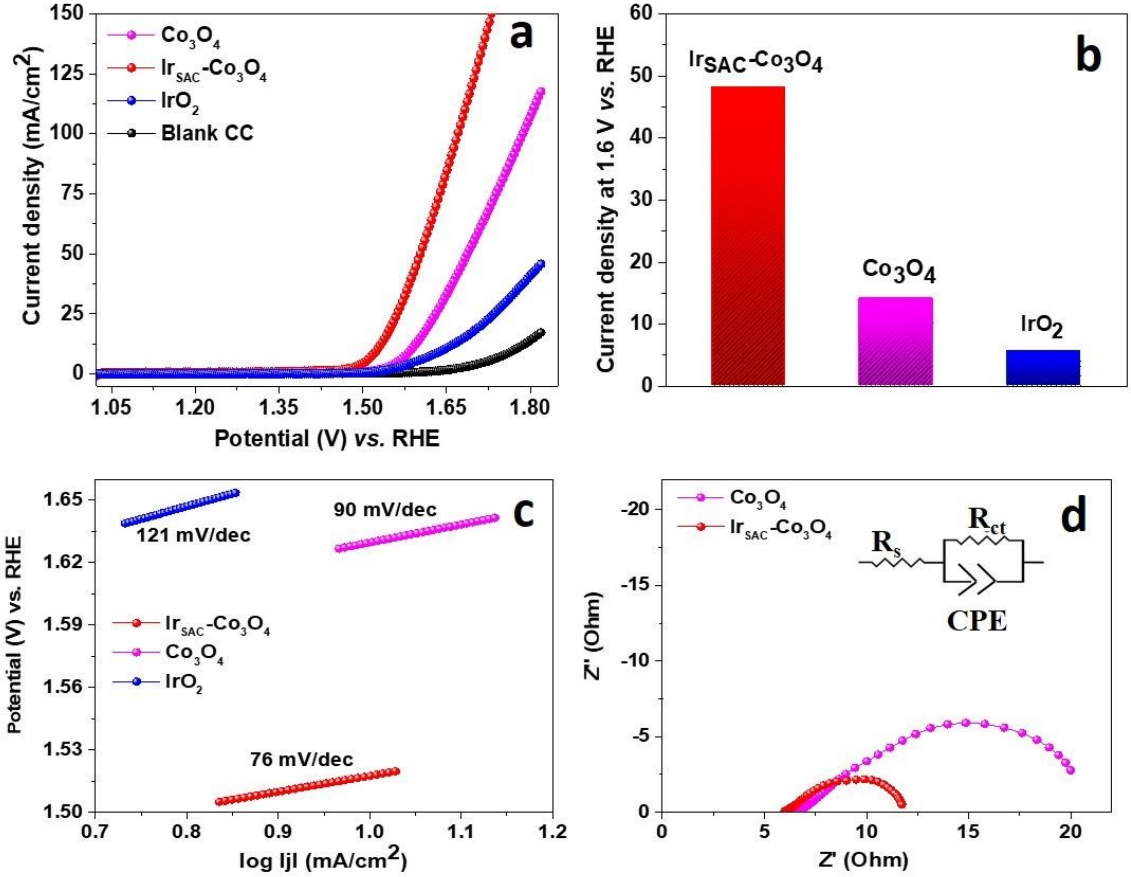

Fig. 4. Electrocatalytic OER activity: LSV polarization curve (a) for blank CC, Co_3O_4, Ir_{SAC}-Co_3O_4, and IrO_2 for OER, (b) histogram plot at 1.6 V *vs.* RHE, (c) Tafel plots of Co_3O_4, Ir_{SAC}-Co_3O_4, and IrO_2, and (d) Nyquist plots of pristine Co_3O_4 and Ir_{SAC}- Co_3O_4

In order to assess the kinetics of the electrode material, the Tafel slope was evaluated using the Tafel equation (given in Supporting Information). The superior reaction kinetics of the Ir_{SAC}-Co_3O_4 reflected by its significantly smaller Tafel slope value (76 mVdec^{-1}) in contrast to Co_3O_4 (90 mVdec^{-1}), and IrO_2 (121 mVdec^{-1}) (Fig. 4c). The faster charge transfer kinetics of Ir_{SAC}-Co_3O_4 was further assessed by the EIS analysis (Table S7). Fig. 4d shows the lower charge transfer resistance (R_{CT}) for the Ir single atom doped sample (5.12 Ω) compared to the pristine Co_3O_4 (12.19 Ω). The lower R_{CT} value of Ir_{SAC}-Co_3O_4 indicates improved kinetics and higher charge transfer efficiency at the electrode-electrolyte interface of the material compared to the pristine Co_3O_4. Furthermore, the lower charge transfer resistance of Ir_{SAC}-Co_3O_4 unveil the close proximity between the electrode and electrolyte. An equivalent circuit with solution resistance (R_S), charge

View Article Online
DOI: 10.1039/D6TA00849F

transfer resistance (R_{CT}), and a constant phase element (CPE) is shown in the inset of Fig. 4d. To further corroborate the enhanced intrinsic activity of Ir_{SAC}-Co_3O_4 for OER, reflected by its lower overpotential and higher mass activity compared to the pristine Co_3O_4 and benchmark IrO_2, TOF was calculated. The obtained TOF values at an overpotential of 370 mV for Ir_{SAC}-Co_3O_4, Co_3O_4, and IrO_2 are 0.03, 0.005, and 0.002 S^{-1}. The TOF value of Ir_{SAC}-Co_3O_4 is 6 times higher than pristine Co_3O_4 and 15 times higher than the benchmark IrO_2. The significantly higher TOF value of Ir_{SAC}-CO_3O_4 compared to both pristine Co_3O_4 and IrO_2 indicates its enhanced intrinsic activity for OER. Table S8 contains a list of all the recorded values of both Co_3O_4 and Ir_{SAC}-Co_3O_4 samples.

Moreover, to calculate the electrochemical active surface area (ECSA), first the electric double layer capacitance (C_{dl}) was evaluated by measuring the CV curves in the non-Faradic potential region (Fig. S7a and b). The double-layer charging current plotted *vs.* the scan rate for both pristine Co_3O_4 and Ir_{SAC}-Co_3O_4 samples at a potential of 1.11 V *vs.* RHE (Fig. S7c). The calculated ECSA values are 12.63 cm^2 and 4.03 cm^2 with a roughness factor of 78.75 and 25.18 for Ir_{SAC}-Co_3O_4 and Co_3O_4, respectively. The enhanced value of ECSA and roughness factor, indicating the elevation in the catalytic active sites and better interaction of reactants with the electrode after the Ir single atom insertion to Co_3O_4 support.

To comprehend the increased activity of Ir_{SAC}-Co_3O_4, CV analysis was carried out and evaluated (Fig. S8). The CV curve can be separated into three different regions. Region (a) signifies the adsorption of $^-$OH ions to the active site. While region (b) contains two simultaneous reactions: oxidation of Co^{2+} to Co^{3+}, active site formation for OER, and the generation of O*, a crucial intermediate that binds with the OH^- group to produce *OOH for oxygen evolution. Finally, the higher potential region (c) consists of the formation of O_2 via the coupling of O–O. The significant decrease in both the peak potential and peak area for Co^{2+}/Co^{3+} in Ir_{SAC}-Co_3O_4 sample related to the Co_3O_4, shows the modified electronic structure of the Co_3O_4 support as a result of strong electronic coupling with Ir single atoms. This electronic coupling accelerates the formation of Co^{2+} to Co^{3+} and the possible surface reconstruction from Co_3O_4 to active CoOOH phase, and thus promotes the OER kinetics by elevating the pre-oxidation process.[35, 47, 48]Lin and co-workers,[49] identified a similar phenomenon of the formation of Ni^{2+} to Ni^{3+} during electrocatalytic OER, which accelerated by the presence of Pt single atoms. Moreover, with the

View Article Online
DOI: 10.1039/D6TA00849F

help of in-situ XAS analysis, Li and co-workers[50] reported the elevated oxidation states of Co and Fe during the OER process.

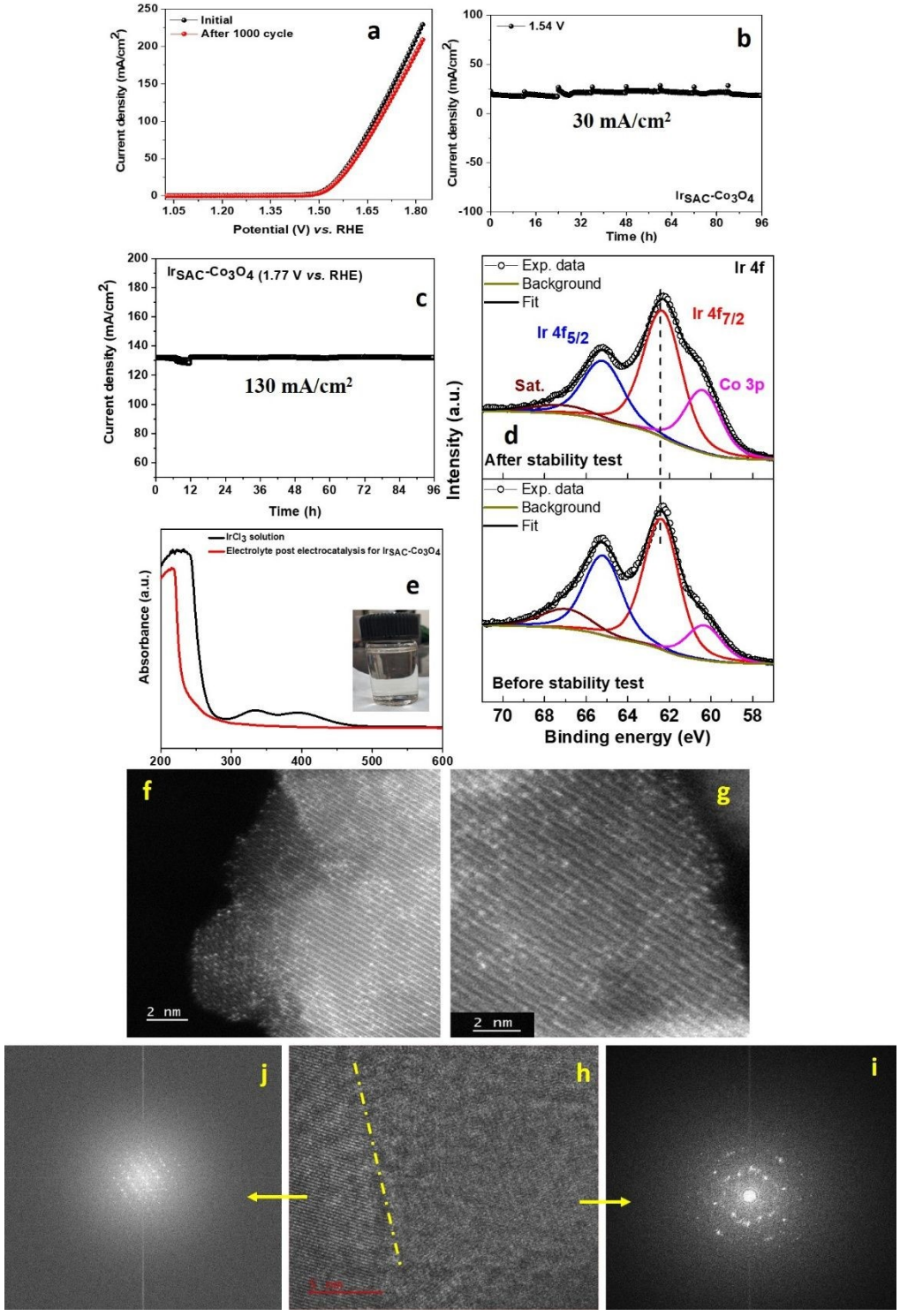

View Article Online
DOI: 10.1039/D6TA00849F

Fig. 5. (a) LSV polarization curve before and after 1000 cycles, chronoamperometry analysis for long-term stability (b) at 1.54 V *vs.* RHE, (c) at 1.77 V *vs.* RHE, and (d) XPS spectra of Ir 4f, before and after stability test for Ir_{SAC}-Co_3O_4 (e) UV spectra of Ir_{SAC}-Co_3O_4 after 24 h electrocatalysis, (f, g) Post-electrocatalysis HAADF-STEM images of Ir_{SAC}-Co_3O_4, (h) HRTEM image of Ir_{SAC}-Co_3O_4 after post electrocatalysis. HRTEM images shows a distinct boundary between highly crystalline Co_3O_4 core and a surface-reconstructed, low crystallinity CoOOH layer. Corresponding FFT image (i) hexagonal symmetry for low crystalline CoOOH phase, and (j) cubic symmetry corresponding to Co_3O_4.

The durability of the Ir_{SAC}-Co_3O_4 of the OER was assessed by 1000 LSV cycles along with the chronoamperometry test. No significant change was observed in the LSV after 1000 cycles (Fig. 5a). Furthermore, chronoamperometry analysis performed at 1.54 V *vs.* RHE shows no evident degradation after 96 h (Fig. 5b). Additionally, the durability of the catalyst was further evaluated at a higher current density of 130 mA/cm² under a fixed potential of 1.77 V. As shown in Fig. 5c, no significant current degradation was observed even after long operational hours, confirming the superior durability of the catalyst at elevated current density and highlighting its potential for industrial applications. This long-term durability further validates the robust electronic interaction of Co_3O_4 support and Ir single atoms, which restrains the aggregation of Ir single atoms throughout the electrocatalysis process. In this regard, He and co-workers reported an extended durability of Ir single atom anchored on $Ni(OH)_2$, which is due to the strong electronic interaction between Ir single atoms and support matrix.[51] The post-electrocatalysis characterizations, FESEM and XPS analysis were performed for the Ir_{SAC}-Co_3O_4. The nanoflower-like morphology of Ir_{SAC}-Co_3O_4 was retained (Fig. S9). Moreover, XPS analysis was used to determine the chemical and electronic states of elements after electrocatalysis. The presence of all elements was confirmed by XPS survey spectra (Fig. S10a). The high-resolution XPS of Co 2p (Fig. S10c) reveals two doublets and three satellite peaks. The binding energy value of Co $2p_{3/2}$ remains constant with peaks at 780.04 and 781.27 eV, and for Co $2p_{1/2}$, peaks appeared at 795.06 and 796.44 eV. Moreover, O 1s binding energy of remains constant, and appears at 530.22, 531.69, and 533.23 eV (Fig. S10b). The binding energy for Ir also stays the same, and appears at 62.31 and 60.44 eV for $4f_{7/2}$ and $4f_{5/2}$, respectively (Fig. 5d). The post-XPS analysis shows that the electronic state of both Co and Ir remains unchanged after the 96 h stability test, which represents the superior robustness of the Ir single atoms on Co_3O_4 support. To further confirm the firmness

View Article Online
DOI: 10.1039/D6TA00849F

of the Ir single atoms on Co_3O_4, ICP-OES analysis of the electrolyte after 24 h of electrocatalysis was performed. The amount of Ir in electrolyte was insignificant which indicates no leaching of Ir atom during catalysis. Moreover, following a 24 h stability test (chronoamperometry analysis), UV-Vis spectrum (Fig. 5e) of the electrolyte exhibits no absorption peak, compare to the UV-Vis spectrum of $IrCl_3$ solution. The presence of two prominent peaks at 375 and 412 nm corresponds to hydrated Ir^{3+} ions in $IrCl_3$ solution. A digital image of the electrolyte after electrocatalysis (inset of Fig. 5e) shows a colorless solution, suggesting no catalyst leaching. Furthermore, post electrocatalysis HAADF-STEM analysis performed to ensure the stability of Ir single atoms on support. The bright, isolated spots corresponding to the Ir single atoms uniformly dispersed across the support matrix (Fig. 5f and g) shows that there is no aggregation of Ir single atoms during the electrocatalysis.

To further gain insight into the possible changes in the catalyst surface after electrocatalysis, HRTEM and FFT analyses were performed following 27 h of chronoamperometry. The post electrocatalysis HRTEM image (Fig. 5h) demonstrates that the sample maintains its highly crystalline lattice fringes for cubic Co_3O_4 phase. However, we also observed the presence of surface reconstructed layer that shows lower crystallinity as compared to Co_3O_4 phase. This region corresponds to the formation of CoOOH active phase during the electrocatalysis. The associated FFT images corresponding to this reconstructed surface region exhibit diffuse diffraction spots that matches with the hexagonal symmetry of the CoOOH (Fig. 5i). Meanwhile, the FFT pattern of crystalline region exhibits the distinct cubic diffraction spots (Fig. 5j), consistent with spinel Co_3O_4. These findings confirm that during electrocatalytic OER the oxide surface reconstructed into the highly active oxyhydroxide phase. The phenomena of surface reconstruction confirmed from HRTEM analysis is well reported in the literature. Li and co-workers, reported similar surface reconstruction of Co-Cr spinel oxides to the CoOOH phase. The surface reconstruction and formation of CoOOH was identified by the post electrocatalysis HRTEM images, where the poor crystalline region emerges due to the formation of active oxy-hydroxide phase during OER.[32] Zou and co-workers, also reported a similar structural evolution of Co_3O_4 to cobalt oxyhydroxide (CoOOH) during OER in 1 M KOH. The presence of CoOOH was validated by the post electrocatalysis HRTEM analysis. The reconstructed surface shows a clear boundary between crystalline Co_3O_4 core and CoOOH shell with different crystallinity.[33] Mori and co-workers, find the amorphous reconstructed layer with the help of both HRTEM and

View Article Online
DOI: 10.1039/D6TA00849F

corresponding FFT images.[52] Along with post-electrocatalysis HRTEM analysis, Raman analysis of Ir_{SAC}-Co_3O_4 sample after 24 and 48 h (chronoamperometry) was analyzed to further verify the surface reconstruction. Ir_{SAC}-Co_3O_4 sample exhibits the characteristic Raman peaks (Fig. S11) at ~677, 608, 512, 189 and 471 cm^{-1}, associated with A_{1g}, three F_{2g} and E_g phonon modes of Co_3O_4, respectively. The A_{1g} and F_{2g} band can be related to the Co^{3+}-O and Co^{2+}-O bond, respectively.[53] The Raman spectra of post electrocatalytic sample exhibits a significant red shift in the peak positions. This shift signifies the weakening of Co-O bonds, formation of oxygen vacancies, and surface reconstruction.[54, 55] Huang and co-workers reported similar red shift to the Raman peak positions for Co_3O_4/CeO_2 after OER. The shift further attributed to the changing in the local bonding environments due to surface reconstruction.[56] Post-electrocatalysis XRD analysis (Fig. S12) shows clear and prominent peaks, which are well matched with Co_3O_4 (JCPDS 00-042-1467). The well-matched 2θ values show there is no change in the crystal structure of the sample. Therefore, all these analyses strengthen the robust electronic interaction and durability of Ir single atoms on the Co_3O_4 support matrix.

5. First-principles DFT Calculations

5.1. Crystal structures of Co_3O_4 and Ir_{SAC}-Co_3O_4 systems

Under ambient pressure (P = 0 GPa), the Co_3O_4 compound exhibits a spinel crystal structure and belongs to face-centered cubic symmetry with space group $Fd\bar{3}m$ and space group number 227. The unit cell of the crystal consists of two non-equivalent Co ions with varying valence configuration viz., Co^{3+} and Co^{2+}. While the four O atoms in the unit cell form several tetrahedral environments by surrounding each Co^{2+} ion, the Co^{3+} ion, on the other hand, is enclosed by six O atoms in order to form octahedral coordination. The optimized crystal structure of Co_3O_4, so attained from the DFT calculations, is shown in Fig. 6(a). The associated optimized lattice parameter of the system is estimated to be ~ 8.046 Å, which is found to match closely with our XRD result (*vide supra*) and other literature as reported elsewhere [57, 58].

To model the Ir_{SAC}-Co_3O_4 compound, a Co atom has been substituted by a single Ir atom on the Co_3O_4 crystal. The substitutional site for Ir in the Co_3O_4 lattice was selected based on the local coordination environment, guided by experimental XAS analyses. Specifically, the coordination number (CN) between Ir and surrounding oxygen atoms has been considered by setting the Ir–O CN to 3 in our model. This choice closely matches our experimental EXAFS

View Article Online
DOI: 10.1039/D6TA00849F

results, which estimate the Ir–O coordination number to be ~3.01, as depicted earlier (*vide supra*). Such a coordination number is characteristic of tetrahedral sites in the spinel Co_3O_4 structure. Co atoms are typically coordinated to three or four oxygen atoms, depending on lattice distortion and relaxation effects. Thus, we assigned Ir substitution at the tetrahedral Co site, as it best reproduces the local structure observed experimentally. The optimized crystal structure of the Ir-$_{SAC}$ Co_3O_4 system with Ir substitution at the tetrahedral Co site is illustrated in Fig. 6.

The defect formation energy (ΔE), as calculated using Equation S1 (Supplementary Information), substantiates the thermodynamic preference between tetrahedral and octahedral sites. The ΔE values for Ir substituted tetrahedral and octahedral sites of Ir_{SAC}-Co_3O_4 are estimated to be -76.61 Ry and -73.44 Ry, respectively, suggesting a favorable structural configuration towards Ir substitution at the tetrahedral Co site with lower ΔE. This result also prioritizes consistency with measured local atomic structure, which is critical for accurately representing the active site geometry of single-atom catalysts. Therefore, the tetrahedral substitution of Ir is both experimentally supported and structurally justified. In this context, it is noteworthy to mention that, within the present DFT framework, additional oxygen vacancies were initially introduced explicitly on the (001) plane of the bare Co_3O_4 system, as illustrated in Fig. S13. The calculated ΔE value for this O-vacant configuration is 79.92 Ry, and its positive magnitude indicates that the oxygen-deficient system is energetically less stable than the pristine Co_3O_4 lattice. Since the lattice parameters and atomic coordinates of the pristine Co_3O_4 structure were directly adopted from experimentally refined crystallographic data, the model inherently reflects the intrinsic oxygen vacancy characteristics typically present in the spinel framework.[59] This modeling strategy ensures that the structural model realistically captures the defect environment observed in Co_3O_4-based systems, thereby maintaining close consistency with experimental conditions. Consequently, to avoid artificial amplification of defect effects and to preserve the intrinsic electronic environment of the system, no additional oxygen vacancies were introduced in the calculations.

View Article Online
DOI: 10.1039/D6TA00849F

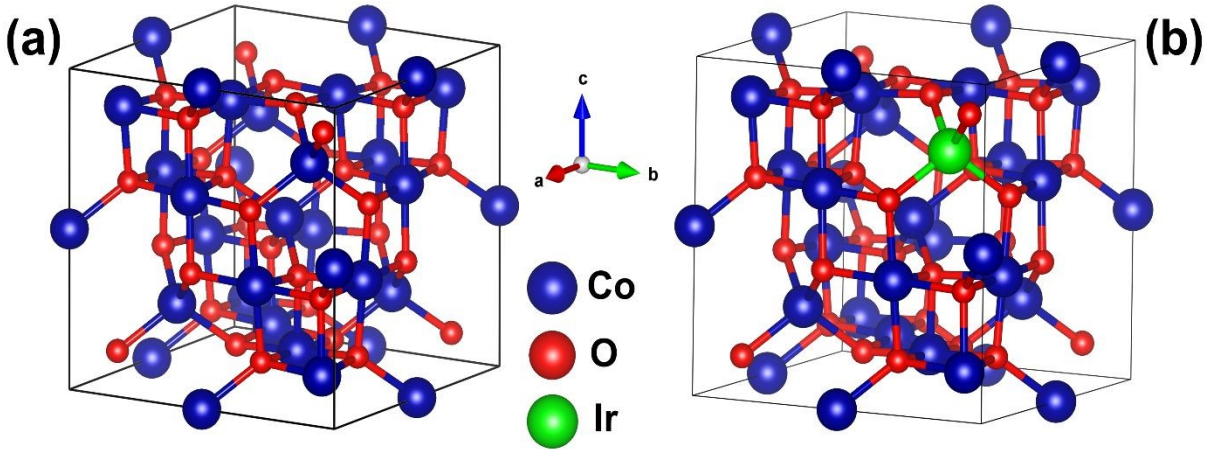

Fig. 6. Optimized crystal structures of **(a)** Co_3O_4 and **(b)** Ir_{SAC}-Co_3O_4 as attained from the DFT calculations.

5.2. Electronic characteristics of Co_3O_4 and Ir_{SAC}-Co_3O_4 systems

The electronic band structures (E-**k** diagrams) of Co_3O_4 and Ir_{SAC}-Co_3O_4 compounds, as estimated from the HSE functional, are shown in Fig. 7A and B, respectively. While the PBE functional is reported to underestimate the band gap (E_g) value of the Co_3O_4 system.[60-62] The PBE+Hubbard-U level of theory is known to overestimate the E_g value of the same compound [60, 61] relative to the experimental result (E_g = 1.60 eV).[63] Considering the fact, the E_g values of the studied compounds have been calculated using the HSE functional with a screening parameter value of 0.20. The HSE functional, in general, is recognized to predict the E_g values of the systems close to the experimental findings.[64-67] From Fig. 7A, it is observed that Co_3O_4 exhibits an indirect (direct) band gap opening along X→W (X→X) high-symmetry direction with E_g value of ~1.60 eV (1.64 eV). The E_g value of the compound, so attained from the HSE functional, is in good agreement with its experimental band gap as reported by Shinde *et al*.[63] Interestingly, distinct band dispersions in E-**k** diagram of Ir_{SAC}-Co_3O_4 material have been observed in Fig. 7B. Significant localization of electronic energy states on the Fermi energy level (E-E_F = 0 eV) indicates that Ir_{SAC}-Co_3O_4 is a conductor with an E_g value of 0 eV. The metallic behavior of Ir_{SAC}-Co_3O_4 further promotes electron transfer efficiency and electrocatalytic activity towards OER performance.[68-70]

View Article Online
DOI: 10.1039/D6TA00849F

The associated orbital resolved PDOS of Co_3O_4 and Ir_{SAC}-Co_3O_4 compounds are depicted in Fig. 7a and b, respectively. The PDOS plots of the systems also reveal their respective semiconducting and metallic behaviors in line with the E-**k** diagrams [Fig. 7(A, B)]. From Fig. 7a, considerable asymmetries between up and down spin channels of PDOS have been reflected, which in turn results in a finite magnetic moment of 3.47 μ_B/cell. The magnetic moment of Co_3O_4, as attained from the HSE functional, is in close agreement with the experimental observation as reported elsewhere.[58] Fig. 7a shows that while the up-spin channel of valence bands ranging from -1.5 to 0 eV for Co_3O_4 system primarily originates from Co^{3+}-4s, Co^{3+}-3d, Co^{2+}-4s and Co^{2+}-3d orbitals, the down spin channel, on the other hand mainly comes from Co^{3+}-3d and Co^{2+}-3d orbitals. However, weak contribution of O-2p orbitals has also been noticed on both the up and down spin channels of valence bands. The up and down spin channels of conduction bands ranging from 0 - 1.5 eV mostly consist of Co^{3+}-3d, Co^{2+}-3d, O-2p and Co^{3+}-3d, Co^{2+}-3d orbitals. Surprisingly, clear symmetries between up and down spin channels of PDOS spectra for the Ir_{SAC}-Co_3O_4 compound have been portrayed in Fig. 7b. This observation shows an early indication of antiferromagnetic behavior of Ir_{SAC}-Co_3O_4 crystal system. From Fig. 7b, definite contribution of Ir-5d atomic orbital has been noticed in addition to Co^{3+}-3d, Co^{2+}-3d and O-2p orbitals on both the up and down spin channels of PDOS. These results collectively suggest that Ir single atom doping is vital in boosting the electrocatalytic performance of the Ir_{SAC}-Co_3O_4 compound, aligning well with our experimental results (*vide supra*). Additionally, upon introduction of Ir single atom, considerable Ir-O and Ir-Co interactions have been found to induce local structural relaxation, as evidenced from the orbital resolved PDOS of Ir_{SAC}-Co_3O_4 compound [Fig. 7(b)]. Owing to the larger atomic radius of Ir compared to O, local lattice distortion occurs, which can effectively suppress some pre-existing oxygen vacancies, thereby lowering their concentration. Similar effects of single atom anchoring leading to vacancy passivation have been reported in other systems.[71, 72] Importantly, despite the reduced oxygen-vacancy concentration, the electronic coupling between Ir atoms and the Co_3O_4 matrix introduces new electronic states and optimizes charge redistribution near the Fermi energy level [Fig. 7(B, b)], which in turn may enhance catalytic activity. Therefore, the increase in OER performance can be ascribed to the synergistic electronic effects and strong coordination of Ir atoms within the Co_3O_4 framework.

The modulation of the electronic structure upon Ir single-atom doping has been further quantified through d-band center analysis derived from the PDOS. For pristine Co_3O_4, the d-band

View Article Online
DOI: 10.1039/D6TA00849F

center values of Co^{3+} and Co^{2+} were located at -1.63 eV and -1.21 eV relative to the Fermi energy level, respectively, indicating relatively deep-lying d states consistent with its semiconducting nature, as also reflected in the E-**k** diagram and PDOS spectra (*cf.* Fig. 7). Upon introduction of Ir single atom, a pronounced shift of the d-band centers was observed, with Co^{3+} shifting to -1.05 eV and 0.44 eV, and Co^{2+} to -0.51 eV and 0.19 eV, while the Ir d-band center values were positioned close to the Fermi energy level (-0.22 eV and 0.29 eV). This significant shift toward the Fermi energy level is attributed to strong orbital hybridization among Ir-5d, Co-3d, and O-2p states, as evidenced by the PDOS results, which show enhanced electronic states near the Fermi energy and a transition from semiconducting to metallic behavior. Such hybridization, coupled with charge redistribution from metal centers to oxygen atoms, leads to a reorganization and broadening of the d states, thereby elevating their energy closer to the Fermi energy level. The upshifted d-band center may imply a strengthening of the interaction between the catalyst surface and oxygenated intermediates, facilitating improved adsorption of *OH and *OOH species while maintaining favorable kinetics for *O formation and O-O bond coupling. Consequently, the optimized positioning of the d-band center in the Ir_{SAC}-Co_3O_4 matrix enables a balanced adsorption-desorption behavior, thereby enhancing the intrinsic electrocatalytic activity toward the oxygen evolution reaction. This analysis, in conjunction with the PDOS observations, confirms that the improved OER performance originates from Ir-induced electronic structure modulation and synergistic coupling within the Co_3O_4 framework rather than solely from pristine Co_3O_4.

View Article Online
DOI: 10.1039/D6TA00849F

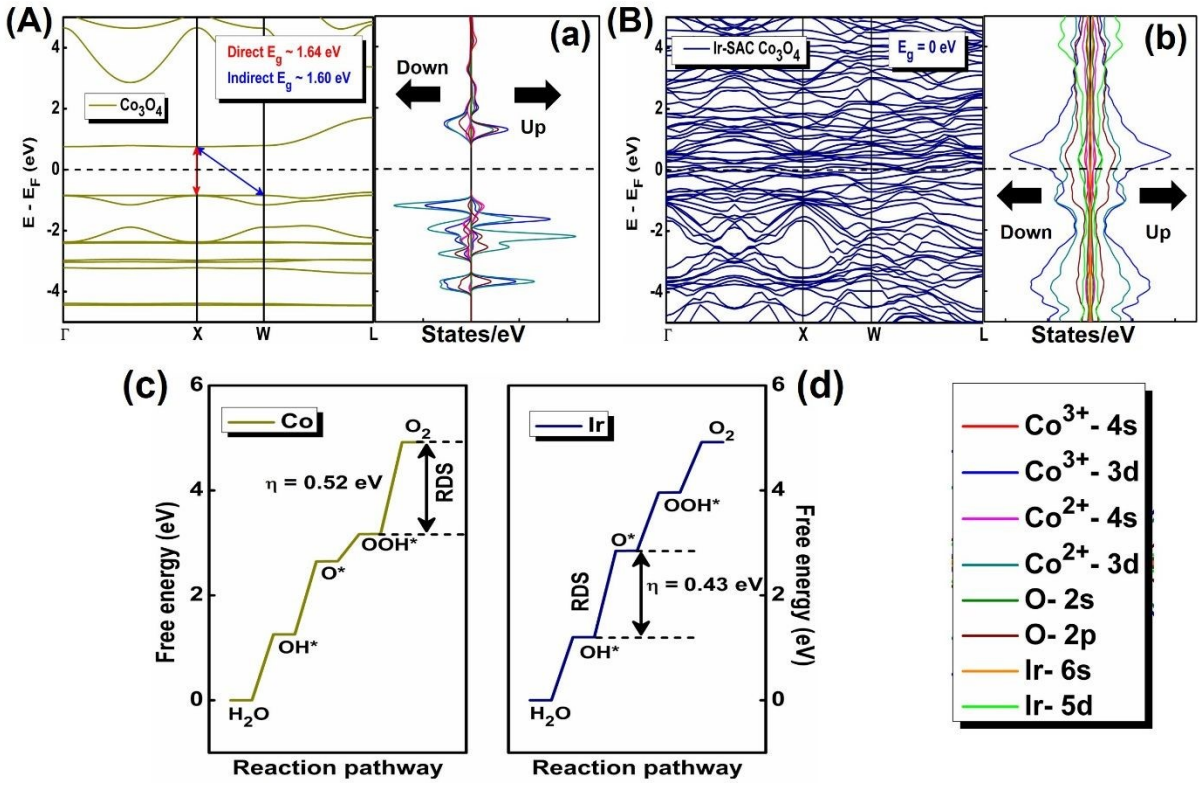

Fig. 7. Electronic band structure of **(A)** Co_3O_4 and **(B)** Ir_{SAC}-Co_3O_4 systems, Orbital resolved PDOS of **(a)** Co_3O_4 and **(b)** Ir_{SAC}-Co_3O_4 compounds [The Fermi energy level is marked at E-E_F = 0 eV. "Up" and "Down" represent up spin and down spin states]. Free energy versus OER pathway for **(c)** Co and **(d)** Ir atomic sites of Co_3O_4 and Ir_{SAC}-Co_3O_4 systems, respectively.

5.3. Charge transfer mechanism and Bader charge analyses in Ir_{SAC}-Co_3O_4 system

To elucidate the electronic interaction between the Ir single atom and Co_3O_4 matrix, Bader charge analysis has been performed. Bader charge difference reveals that Ir and Co atoms undergo electron depletion of +0.86 e and +0.50 e, respectively, while oxygen atoms exhibit electron accumulation of -1.35 e. This charge redistribution indicates that electrons are transferred from the transition metal centers to the surrounding oxygen atoms, leading to the formation of electron-deficient Ir and Co species and electron-enriched O sites. Such behavior suggests that the incorporation of the Ir single atom induces significant electronic perturbation within the Co_3O_4 crystal system, with Ir acting as a dominant charge modulation center. The resulting charge polarization is facilitated through strong Ir-O-Co interactions, giving rise to enhanced metal-oxygen co-valency and orbital hybridization. This interpretation is further supported by the orbital-

View Article Online
DOI: 10.1039/D6TA00849F

resolved PDOS results (*vide supra, cf*. Section 5.2), wherein notable contributions from Ir-5d states in conjunction with Co-3d and O-2p orbitals near the Fermi energy level confirm strong electronic coupling and redistribution of electronic states upon Ir incorporation. The increased O-2p participation near the Fermi energy level is consistent with the observed electron accumulation on oxygen atoms, indicating improved charge delocalization across the lattice. Consequently, the formation of electron-rich oxygen sites is expected to promote proton-coupled electron transfer and stabilize key OER intermediates (*OH and *OOH), while the electron-deficient Ir center may enhance the electrophilic character of the active site, facilitating *O formation and subsequent O-O bonding. In addition, the partial oxidation of Co sites further tunes the adsorption energetics, enabling an optimal balance between intermediate binding strength and reaction kinetics. Therefore, the enhanced OER activity of the Ir_{SAC}-Co_3O_4 compound is attributed to the synergistic electronic coupling and charge redistribution induced by Ir single atom.

5.4. Electrochemical reaction pathway and active site(s) for OER

To better understand the electrocatalytic water-splitting process and active site(s) for OER, free energy changes were calculated as a function of the electrochemical reaction pathway. The calculations were performed for Co and Ir atomic sites of Co_3O_4 and Ir_{SAC}-Co_3O_4 compounds, respectively. Fig. 7c and d show the results. Each site's overpotential (η) value was calculated for its rate-determining step (RDS). Although the RDS for the Co atomic site of Co_3O_4 can be estimated from the formation of O_2, the RDS for the Ir site of the Ir_{SAC}-Co_3O_4 system is correlated with the oxidation of OH* in the OER process.[73-75] From Fig. 7c and d, the η values of Co and Ir atomic sites in Co_3O_4 and Ir_{SAC}-Co_3O_4 systems have been estimated to be 0.35 and 0.26 eV, respectively. The minimum η for Ir site of Ir_{SAC}-Co_3O_4 compound indicates the efficacy of Ir SAC as the predominant active site for OER mechanism.

The binding energy difference of oxygen intermediates is directly linked with η values of the atomic sites.[76] From Fig. 7c and d, the binding energy differences for OOH* - O_2 and OH* - O* intermediates of Co and Ir atomic sites along the reaction pathway are found to be 0.35 and 0.26 eV, respectively. This observation not only suggests that Ir active site possesses lower binding energy in contrast to Co site, but also shows that the estimated binding energy difference (= 0.26 eV) falls under the optimal values of binding energy for OER activity elsewhere.[77-80] The overall results portray that Ir single atom doping on Co_3O_4 enhances the OER performance towards an

View Article Online
DOI: 10.1039/D6TA00849F

improved electrocatalytic water-splitting mechanism in line with the experimental observations (*vide supra*).

In this connection, it may be relevant to mention that the mechanistic interpretation of the OER pathway can also be correlated with experimental electrochemical data. The Tafel slope obtained for the Ir_{SAC}-Co_3O_4 system is 76 mV/dec, indicative of a RDS involving the OH* to O*, as suggested by classical electro kinetic models for alkaline OER. This observation is in good agreement with the DFT results, which identify the OH* → O* transition as the RDS on the Ir site, with an associated overpotential of 0.26 eV, lower than that of the Co site in pristine Co_3O_4. The reduced energy barrier and optimized binding energy difference of OH*–O* on the Ir center suggest that Ir substitution enhances the OER kinetics by stabilizing key intermediates and lowering the energy requirement for the rate-limiting step. This mechanistic correlation between theoretical predictions and experimental electrochemical data underscores the significance of Ir-SAC doping in promoting OER activity.

Conclusions

To summarize, a three-step process was used to synthesize an Ir single-atom catalyst on Co_3O_4 support. The first phase is the hydrothermal process, which involves the formation of a cobalt-carbonate-hydroxide complex, followed by the impregnation of Ir ions over the metal hydroxide complex and subsequently calcination, which results in Ir single atoms on Co_3O_4 support. XRD of the synthesized sample confirms the formation of the pure phase of Co_3O_4. Moreover, no diffraction peak corresponding to the IrO_2 and metallic Ir is observed. FESEM analysis confirms a nanoflower morphology with edge lengths ranging from 100 to 400 nm. The vertically grown nanoflower morphology and rough surface are highly active for electrocatalytic OER. Furthermore, the presence of single atoms is validated by HAADF-STEM images and XAS analysis. The HAADF-STEM mapping confirmed an atomic distribution of Ir single atoms on the substrate matrix. EXAFS analysis shows no peak of Ir-Ir bond for Ir_{SAC}-Co_3O_4 sample, providing a strong affirmation for the existence of Ir single atoms. These single atoms stabilized on the Co_3O_4 support matrix via interacting with the support atoms and form Ir-O, and Ir-Co bond pairs. The bonding results in strong electronic coupling between the Ir single atoms and Co_3O_4 matrix that modifies the electronic state of Ir and leads to its increased density of unoccupied orbitals. Furthermore, the valence state of Co atoms is enhanced as a result of electronic interaction with

View Article Online
DOI: 10.1039/D6TA00849F

highly oxidized Ir single atoms, which further strengthens the overall electrocatalytic performance of the material. Consequently, the improved electrocatalytic OER efficiency results from the combined synergistic interaction of the support matrix and Ir single atoms. An adequate loading of Ir (3.04 wt%) was observed with the help of ICP-OES analysis. The synthesized Ir_{SAC}-Co_3O_4 shows improved OER activity in alkaline medium, exhibiting an onset potential of 1.51 V *vs.* RHE to generate 10 mA/cm^2 current density with a stability up to 96 h. This extended durability of Ir_{SAC}-Co_3O_4 demonstrates that Ir single atoms do not aggregate throughout the electrocatalysis. The calculated TOF value for Ir_{SAC}-Co_3O_4 is 0.03 S^{-1}, which is 15 times higher than the benchmark IrO_2. Post-electrocatalytic XPS analysis shows no substantial change in the oxidation state of Ir single atoms as well Co atoms of the support matrix. Furthermore, post-electrocatalytic ICP-OES analysis confirms no leaching of Ir atoms into the electrolyte. Both results demonstrate the robust electronic coupling between single atoms and the support matrix. The calculated optimized binding energy values of intermediates during OER by DFT calculation revealed an optimum binding energy for Ir sites, indicating that Ir is an active site for OER. Therefore, this work demonstrates an anchoring of a single atom Iridium on Co_3O_4 support with a strong synergistic electronic coupling, which indeed improve the electrocatalytic performance towards OER in alkaline conditions.

Supporting Information

Instrumental information, list of chemicals, calculation for all the analysis, computational details, XRD of samples, pristine Co_3O_4 and Ir single atom doped Co_3O_4, FESEM, TEM, and XPS of pristine material, XAS fitting result, EPR analysis, HAADF-STEM image and mapping analysis, optimization of electrocatalytic activity, CV and C_{dl} measurement of Co_3O_4 and Ir_{SAC}-Co_3O_4, post electrocatalysis FESEM, XPS, and Raman analysis. Crystal structure of oxygen vacant system.

View Article Online
DOI: 10.1039/D6TA00849F

Author contributions:

Astha Gupta: Conceptualization, overall research work, data acquisition, formal analysis, and manuscript writing, and editing. **Swarup Ghosh**: Computational work, writing and editing. **Dinesh Bhalothia**: Data curation and formal analysis. **Joydeep Chowdhury**: Writing, and editing. **Surojit Pande**: Overall design of research idea, data acquisition, formal analysis, supervision, funding acquisition, manuscript writing, and editing.

Conflict of interest: The authors declare no conflict of interest.

Acknowledgments:

Surojit Pande thanks the financial support from the Science and Engineering Research Board (SERB) under sanction number CRG/2023/001368. Astha Gupta expresses gratitude to BITS Pilani, Pilani campus, for their financial support. We'd also like to thank BITS Pilani's Central Instrument Facility (CIF) for providing access to the FESEM and XPS analysis. We would also like to thank BITS Pilani's Central Instrument Facility (CIF) for granting access to the FESEM and XPS analyses. The researchers also acknowledge the Biology Department at BITS Pilani for carrying out the ICP analysis. We would also like to thank Dr. Biplab Ghosh and Dr. Rajashri Urkude from the Raja Ramanna Centre for Advanced Technology (RRCAT) in Indore, India, for conducting the XAS analysis at the BL-09 Scanning EXAFS beamline, Indus-2 Synchrotron. We would like to acknowledge the SATHI Facility at IIT Kharagpur for the HAADF-STEM analysis. Authors would like to thank the National Supercomputing Mission (NSM) for providing computing resources of 'PARAM Kamrupa' at IIT Guwahati, which is implemented by C-DAC and supported by the Ministry of Electronics and Information Technology (MeitY) and Department of Science and Technology (DST), Government of India. Dinesh Bhalothia acknowledges the funding support (Enhanced Seed Grant EF/2024-25/QE-04-08) from Manipal University Jaipur. Swarup Ghosh also acknowledges Bioinformatics Resources and Applications Facility (BRAF), C-DAC, Pune for using a part of computational work.

View Article Online
DOI: 10.1039/D6TA00849F

References:

1. D. Rathore, M. D. Sharma, A. Sharma, M. Basu and S. Pande, *Langmuir*, 2020, **36**, 14019-14030.
2. B. You and Y. Sun, *Acc. Chem. Res.*, 2018, **51**, 1571-1580.
3. N.-T. Suen, S.-F. Hung, Q. Quan, N. Zhang, Y.-J. Xu and H. M. Chen, *Chem. Soc. Rev.*, 2017, **46**, 337-365.
4. S. Anantharaj, S. R. Ede, K. Sakthikumar, K. Karthick, S. Mishra and S. Kundu, *ACS Catal.*, 2016, **6**, 8069-8097.
5. M. Kim, J. Park, M. Kang, J. Y. Kim and S. W. Lee, *ACS Cent Sci.*, 2020, **6**, 880-891.
6. M. Basu, *J. Colloid Interface Sci.*, 2018, **530**, 264-273.
7. C. Mahala, M. D. Sharma and M. Basu, *Electrochim. Acta*, 2018, **273**, 462-473.
8. Y. Zhan, G. Du, S. Yang, C. Xu, M. Lu, Z. Liu and J. Y. Lee, *ACS Appl. Mater. Interfaces*, 2015, **7**, 12930-12936.
9. O. Diaz-Morales, I. Ledezma-Yanez, M. T. Koper and F. Calle-Vallejo, *Acs Catalysis*, 2015, **5**, 5380-5387.
10. R. Elakkiya and G. Maduraiveeran, *Nanoscale*, 2021, **13**, 14837-14846.
11. Y. Guo, T. Park, J. W. Yi, J. Henzie, J. Kim, Z. Wang, B. Jiang, Y. Bando, Y. Sugahara and J. Tang, *Adv. Mater.*, 2019, **31**, 1807134.
12. G. Yuan, J. Bai, L. Zhang, X. Chen and L. Ren, *Appl. Catal. B*, 2021, **284**, 119693.
13. Z. Liu, X. Ning, A. Hao, M. F. Khan and S. Rehman, *ChemSusChem*, 2025, **18**, e202401197.
14. X. Xu, P. Du, Z. Chen and M. Huang, *J. Mater. Chem. A*, 2016, **4**, 10933-10939.
15. F. Abdelghafar, X. Xu, D. Guan, Z. Lin, Z. Hu, M. Ni, H. Huang, T. Bhatelia, S. P. Jiang and Z. Shao, *ACS Mater. Lett.*, 2024, **6**, 2985-2994.
16. X. Xu, Y. Pan, L. Ge, Y. Chen, X. Mao, D. Guan, M. Li, Y. Zhong, Z. Hu, V. K. Peterson, M. Saunders, C.-T. Chen, H. Zhang, R. Ran, A. Du, H. Wang, S. P. Jiang, W. Zhou and Z. Shao, *Small*, 2021, **17**, 2101573.
17. X.-F. Yang, A. Wang, B. Qiao, J. Li, J. Liu and T. Zhang, *Acc. Chem. Res.,* 2013, **46**, 1740-1748.
18. L. Liu and A. Corma, *Chem. Rev.*, 2018, **118**, 4981-5079.
19. H. Zhang, G. Liu, L. Shi and J. Ye, *Adv. Energy Mater.*, 2018, **8**, 1701343.
20. J. Li, G. Fu, X. Sheng, G. Li, H. Chen, K. Shu, Y. Dong, T. Wang and Y. Deng, *Adv. Powder Mater.*, 2024, **3**, 100227.
21. T. Wei, J. Zhou and X. An, *Mater. Rep. Energy*, 2024, **4**, 100285.
22. Y. Zhou, Y. Jiang, Y. Ji, R. Lang, Y. Fang and C. D. Wu, *ChemCatChem*, 2023, **15**, e202201176.
23. J. Li, C. Chen, L. Xu, Y. Zhang, W. Wei, E. Zhao, Y. Wu and C. Chen, *J. Am. Chem. Soc. Au*, 2023, **3**, 736-755.
24. M. B. Gawande, P. Fornasiero and R. Zbořil, *Acs Catal.*, 2020, **10**, 2231-2259.
25. Q. Wang, Z. Zhang, C. Cai, M. Wang, Z. L. Zhao, M. Li, X. Huang, S. Han, H. Zhou and Z. Feng, *J. Am. Chem. Soc.*, 2021, **143**, 13605-13615.
26. P. Zhai, M. Xia, Y. Wu, G. Zhang, J. Gao, B. Zhang, S. Cao, Y. Zhang, Z. Li and Z. Fan, *Nature Commun.*, 2021, **12**, 4587.
27. A. Gupta, S. Ghosh, D. Bhalothia, S. Thangarasu, B. Ghosh, R. Urkude, J. Chowdhury and S. Pande, *J. Mater. Chem. A*, 2024, **12**, 23819-23836.

View Article Online
DOI: 10.1039/D6TA00849F

28. R. Lang, X. Du, Y. Huang, X. Jiang, Q. Zhang, Y. Guo, K. Liu, B. Qiao, A. Wang and T. Zhang, *Chem. Rev.*, 2020, **120**, 11986-12043.
29. R. Li, L. Luo, X. Ma, W. Wu, M. Wang and J. Zeng, *J. Mater. Chem. A*, 2022, **10**, 5717-5742.
30. K. Tan, M. Dixit, J. Dean and G. Mpourmpakis, *Ind. Eng. Chem. Res.*, 2019, **58**, 20236-20246.
31. Z. Yan, B. Yao, C. Hall, Q. Gao, W. Zang, H. Zhou, Q. He and H. Zhu, *Nano Lett.*, 2022, **22**, 8122-8129.
32. B. He, P. Hosseini, T. Priamushko, O. Trost, E. Budiyanto, C. Bondue, J. Schulwitz, A. Kostka, H. Tüysüz, M. Muhler, S. Cherevko, K. Tschulik and T. Li, *Nature Commun.*, 2025, **16**, 9895.
33. R. Zhang, L. Pan, B. Guo, Z.-F. Huang, Z. Chen, L. Wang, X. Zhang, Z. Guo, W. Xu, K. P. Loh and J.-J. Zou, *J. Am. Chem. Soc.*, 2023, **145**, 2271-2281.
34. A. Kumar, M. Gil-Sepulcre, J. P. Fandré, O. Rüdiger, M. G. Kim, S. DeBeer and H. Tüysüz, *J. Am. Chem. Soc.*, 2024, **146**, 32953-32964.
35. M.-Q. Yang, K.-L. Zhou, C. Wang, M.-C. Zhang, C.-H. Wang, X. Ke, G. Chen, H. Wang and R.-Z. Wang, *J. Mater. Chem. A*, 2022, **10**, 25692-25700.
36. C. Cai, M. Wang, S. Han, Q. Wang, Q. Zhang, Y. Zhu, X. Yang, D. Wu, X. Zu and G. E. Sterbinsky, *ACS Catal.*, 2020, **11**, 123-130.
37. J. Shan, C. Ye, S. Chen, T. Sun, Y. Jiao, L. Liu, C. Zhu, L. Song, Y. Han and M. Jaroniec, *J. Am. Chem. Soc.*, 2021, **143**, 5201-5211.
38. W. Zhao, F. Xu, J. Yang, X. Hu and B. Weng, *Inorg. Chem.*, 2024, **63**, 1947-1953.
39. D. Bhalothia, Y.-M. Yu, Y.-R. Lin, T.-H. Huang, C. Yan, J.-F. Lee, K.-W. Wang and T.-Y. Chen, *Sustain. Energy Fuel.*, 2021, **5**, 5490-5504.
40. P. Hu, Z. Huang, Z. Amghouz, M. Makkee, F. Xu, F. Kapteijn, A. Dikhtiarenko, Y. Chen, X. Gu and X. Tang, *Angew. Chem. Int. Ed.*, 2014, **53**, 3418-3421.
41. N. Cheng, S. Stambula, D. Wang, M. N. Banis, J. Liu, A. Riese, B. Xiao, R. Li, T.-K. Sham and L.-M. Liu, *Nature commun.*, 2016, **7**, 13638.
42. L. Zhang, R. Si, H. Liu, N. Chen, Q. Wang, K. Adair, Z. Wang, J. Chen, Z. Song and J. Li, *Nature commun.*, 2019, **10**, 4936.
43. J. Yin, J. Jin, M. Lu, B. Huang, H. Zhang, Y. Peng, P. Xi and C.-H. Yan, *J. Am. Chem. Soc.*, 2020, **142**, 18378-18386.
44. L. Liu, Z. Jiang, L. Fang, H. Xu, H. Zhang, X. Gu and Y. Wang, *ACS Appl. Mater. Interfaces*, 2017, **9**, 27736-27744.
45. S. Biswal, B. Mishra, D. Pohl, B. Rellinghaus, D. Ghosh and B. P. Tripathi, *J. Mater. Chem. A*, 2024, **12**, 2491-2500.
46. D. Rathore, S. Ghosh, A. Gupta, J. Chowdhury and S. Pande, *ACS Appl. Nano Mater.*, 2024, **7**, 9730-9744.
47. K. L. Zhou, Z. Wang, C. B. Han, X. Ke, C. Wang, Y. Jin, Q. Zhang, J. Liu, H. Wang and H. Yan, *Nature Commun.*, 2021, **12**, 3783.
48. B. He, F. Bai, P. Jain and T. Li, *Small*, 2025, **21**, 2411479.
49. C. Lin, Y. Zhao, H. Zhang, S. Xie, Y.-F. Li, X. Li, Z. Jiang and Z.-P. Liu, *Chem. Sci.*, 2018, **9**, 6803-6812.
50. P. Li, M. Wang, X. Duan, L. Zheng, X. Cheng, Y. Zhang, Y. Kuang, Y. Li, Q. Ma and Z. Feng, *Nature Commun.*, 2019, **10**, 1711.

View Article Online
DOI: 10.1039/D6TA00849F

51. Q. He, S. Qiao, Q. Zhou, Y. Zhou, H. Shou, P. Zhang, W. Xu, D. Liu, S. Chen and X. Wu, *Nano Lett.*, 2022, **22**, 3832-3839.
52. S. Yagi, I. Yamada, H. Tsukasaki, A. Seno, M. Murakami, H. Fujii, H. Chen, N. Umezawa, H. Abe, N. Nishiyama and S. Mori, *Nature Commun.*, 2015, **6**, 8249.
53. R. Madhu, A. Karmakar, P. Arunachalam, J. Muthukumar, P. Gudlur and S. Kundu, *J. Mater. Chem. A*, 2023, **11**, 21767-21779.
54. C. Pasquini, L. D'Amario, I. Zaharieva and H. Dau, *J. Chem. Phys.*, 2020, **152**.
55. B. S. Yeo and A. T. Bell, *J. Am. Chem. Soc.*, 2011, **133**, 5587-5593.
56. J. Huang, H. Sheng, R. D. Ross, J. Han, X. Wang, B. Song and S. Jin, *Nature Commun.*, 2021, **12**, 3036.
57. W. L. Smith and A. D. Hobson, *Acta Cryst. B*, 1973, **29**, 362-363.
58. W. L. Roth, *J. Phys. Chem. Solids.* , 1964, **25**, 1-10.
59. Z.-H. Yin, H. Liu, J.-S. Hu and J.-J. Wang, *Natl. Sci. Rev.*, 2024, **11**, nwae362.
60. J. Chen, X. Wu and A. Selloni, *Phys. Rev. B*, 2011, **83**, 245204.
61. I. Kim, H.-H. Nahm and M. Choi, *Curr. Appl. Phys.*, 2021, **22**, 65-70.
62. A. F. Lima, *J. Phys. Chem. Solids.*, 2014, **75**, 148-152.
63. V. R. Shinde, S. B. Mahadik, T. P. Gujar and C. D. Lokhande, *Appl. Surf. Sci.*, 2006, **252**, 7487-7492.
64. S. Ghosh and J. Chowdhury, *RSC Adv.*, 2024, **14**, 6385-6397.
65. S. Ghosh and J. Chowdhury, *Mod. Phys. Lett. B*, 2023, **38**, 2330003.
66. S. Ghosh and J. Chowdhury, *Mater Sci Eng B.*, 2022, **284**, 115903.
67. S. Ghosh, S. Sarkar and J. Chowdhury, *Mater. Chem. Phys.*, 2022, **276**, 125379.
68. D. Rathore, S. Ghosh, A. Gupta, J. Chowdhury and S. Pande, *ACS Appl. Nano Mater.*, 2024, **7**, 9730-9744.
69. D. Rathore, S. Ghosh, J. Chowdhury and S. Pande, *ACS Appl. Nano Mater.*, 2023, **6**, 3095-3110.
70. D. Rathore, S. Ghosh, J. Chowdhury and S. Pande, *ACS Appl. Nano Mater.*, 2022, **5**, 11823-11838.
71. X. Wang, D. Santos-Carballal and N. H. de Leeuw, *J. Chem. Phys.*, 2024, **160**, 154713.
72. S. Chandrappa, S. J. Galbao, P. S. Sankara Rama Krishnan, N. A. Koshi, S. Das, S. N. Myakala, S.-C. Lee, A. Dutta, A. Cherevan, S. Bhattacharjee and D. H. K. Murthy, *J. Phys. Chem. C*, 2023, **127**, 12383-12393.
73. N. Dubouis and A. Grimaud, *Chem. Sci.*, 2019, **10**, 9165-9181.
74. M. Irshad, M. H. U. R. Mahmood and M. Fatima, in *Graphene, Nanotubes and Quantum Dots-Based Nanotechnology*, ed. Y. Al-Douri, Woodhead Publishing, 2022, pp. 537-556.
75. S. F. Zai, X. Y. Gao, C. C. Yang and Q. Jiang, *Adv. Energy Mater.*, 2021, **11**, 2101266.
76. B. You, M. T. Tang, C. Tsai, F. Abild-Pedersen, X. Zheng and H. Li, *Adv. Mater.*, 2019, **31**, 1807001.
77. B. Hinnemann, P. G. Moses, J. Bonde, K. P. Jørgensen, J. H. Nielsen, S. Horch, I. Chorkendorff and J. K. Nørskov, *J. Am. Chem. Soc.*, 2005, **127**, 5308-5309.
78. I. C. Man, H.-Y. Su, F. Calle-Vallejo, H. A. Hansen, J. I. Martínez, N. G. Inoglu, J. Kitchin, T. F. Jaramillo, J. K. Nørskov and J. Rossmeisl, *ChemCatChem*, 2011, **3**, 1159-1165.
79. S. Sun, X. Zhou, B. Cong, W. Hong and G. Chen, *ACS Catal.*, 2020, **10**, 9086-9097.
80. J. Li, *Nano-Micro Lett.*, 2022, **14**, 112.

View Article Online
DOI: 10.1039/D6TA00849F

Data Availability Statement

Scheme 1: Power point presentation

Figure 1: Electron microscopy characterisation: ImageJ software

Figure 2. X-ray absorption spectroscopy analysis: Athena and Artemis software

Figure 3. X-ray photoelectron spectroscopy: Casa XPS, Thermo Avantage software, OriginPro 9.0

Figure 4, and 5. OriginPro 9.0 software

Figure 6. and 7: Quantum ESPRESSO (version 7.1) software. Visualization: Vesta and OriginPro 9.0.

All data supporting the findings of this study are available within the paper and ESI file.